

Manuscript accepted at Earth and Planetary Science Letters, doi: 10.1016/j.epsl.2017.07.004

Deglacial changes in flow and frontal structure through the Drake Passage

Authors: J. Roberts^{1,2*}, I.N. McCave¹, E.L. McClymont³, S. Kender^{4,5}, C.-D. Hillenbrand², R. Matano⁶, D.A. Hodell¹, V.L. Peck²

Affiliations: ¹ Godwin Laboratory for Palaeoclimate Research, Department of Earth Sciences, University of Cambridge, Downing Street, Cambridge, CB2 3EQ; ² British Antarctic Survey, High Cross, Madingley Road, Cambridge, CB3 0ET; ³ Department of Geography, Durham University, South Road, Durham, DH1 3LE; ⁴ Camborne School of Mines, University of Exeter, Penryn Campus, Penryn, Cornwall TR10 9FE UK; ⁵ British Geological Survey, Nicker Hill, Keyworth, Nottingham, NG12 5GG; ⁶ College of Oceanic and Atmospheric Sciences, Oregon State University, Corvallis, Oregon, USA;

*Now based at the Alfred-Wegener-Institut, Helmholtz-Zentrum für Polar- und Meeresforschung, Am Alten Hafen 26, 27568 Bremerhaven

Correspondence to: jenny.roberts@awi.de

Keywords: Cold Water Route; Sortable Silt; Deglacial; Alkenones; Sub-Antarctic Front

Abstract: The oceanic gateways of the Drake Passage and the Agulhas Current are critical locations for the inflow of intermediate-depth water masses to the Atlantic, which contribute to the shallow return flow that balances the export of deep water from the North Atlantic. The thermohaline properties of northward flowing intermediate water are ultimately determined by the inflow of water through oceanic gateways. Here, we focus on the less well-studied “Cold Water Route” through the Drake Passage. We present millennially-resolved bottom current flow speed and sea surface temperature records downstream of the Drake Passage spanning the last 25,000 years. We find that prior to 15 ka, bottom current flow speeds at sites in the Drake Passage region were dissimilar and there was a marked anti-phasing between sea surface temperatures at sites upstream and downstream of the Drake Passage. After 14 ka, we observe a remarkable convergence of flow speeds coupled with a sea surface temperature phase change at sites upstream and downstream of Drake Passage. We interpret this convergence as evidence for a significant southward shift of the sub-Antarctic Front from a position north of Drake Passage. This southward shift increased the through-flow of water from the Pacific, likely reducing the density of Atlantic Intermediate Water. The timing of the southward shift in the sub-Antarctic Front is synchronous with a major re-invigoration of Atlantic Meridional Overturning Circulation, with which, we argue, it may be linked.

Introduction

The export of North Atlantic Deep Water (NADW) to the South Atlantic requires a compensating intermediate-depth northward flow. Volume transport estimates suggest that Antarctic Intermediate Water (AAIW) is the main component of this upper layer return flow (Poole and Tomczak, 1999). Thermocline waters contributing to Atlantic AAIW enter the Atlantic either through Drake Passage (the Cold Water Route) or via the Agulhas Current (the Warm Water Route) (Poole and Tomczak, 1999). The water mass properties of these AAIW contributions are markedly different, with relatively cold-fresh water entering the southwest Atlantic via the Cold Water Route and warmer-saltier thermocline waters entering the southeast Atlantic via the Warm Water Route (Gordon et al., 1992). The relative contribution and thermohaline properties of these water masses determine the Atlantic's meridional heat and freshwater fluxes, and thus have implications for global climate.

Whilst there have been a large number of studies that have focused on the changes in the flow and thermohaline properties of water masses entering the southeast Atlantic via the Warm Water Route, there are relatively few proxy reconstructions of past changes in Cold Water Route inflow.

The inflow of water via the Cold Water Route is strongly influenced by the position of the oceanic fronts within the Drake Passage. Low-density Sub-Antarctic Mode Water (SAMW), formed in the southeast Pacific, is transported into the Atlantic basin north of the sub-Antarctic Front (SAF, the most northerly jet of the Antarctic Circumpolar Current, ACC) (Talley, 1999). Along its flow path through the Drake Passage, SAMW mixes with Antarctic-derived waters to ultimately form the cold-fresh AAIW end-member in the Atlantic. Determining the position of the SAF is therefore critical for understanding changes in the inflow of low-density intermediate water via the Cold Water Route in the past.

Sea surface temperature (SST)-based reconstructions of the SAF during the last glacial period suggest that it was 5-10° northwards of its present position (e.g. Gersonde et al., 2005); however, reconstructions of the position of the SAF in the Drake Passage region remain scarce. Estimates of bottom current speed (McCave et al., 1995) provide a more direct means to determine relative changes in Cold Water Route through-flow. To-date, the only two flow speed reconstructions from within (Lamy et al., 2015) and downstream (McCave et al., 2014) of the Drake Passage are relatively low resolution across the last deglaciation and their interpretation of deglacial changes in flow via the Cold Water Route are contradictory.

Here, we use a multi-proxy approach to determine changes in the structure and flow of water through the Cold Water Route over the last deglaciation. We present sub-millennially-resolved bottom current flow speed and alkenone-based SST reconstructions from a site immediately downstream of Drake Passage spanning the last 25 kyr. Comparison with other SST and bottom current flow speed records from the Drake Passage region reveals that the Last Glacial Maximum (LGM) and early deglacial was characterised by a very different spatial pattern of SSTs and bottom current flow speeds relative to the last 14 kyr, suggesting Cold Water Route through-flow during the glacial period was reduced.

2. Materials and Methods

2.1 Core Material

This study is based on the sediment core GC528 (53°0.8'S, 58°2.4'W, 598 m) located on the southern flank of the Falkland Plateau collected on the cruise JR244 of the RRS *James Clark Ross*. The core was taken from a contourite drift (South Falkland Slope Drift; Koenitz et al., 2008), that is today located under the core of a strong westerly jet associated with the SAF (Figure 1) and is bathed by AAIW.

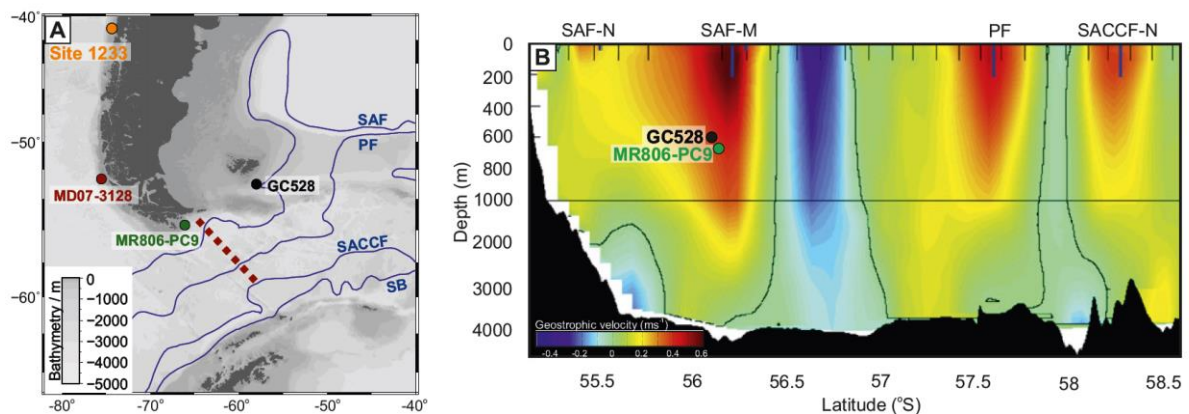


Figure 1: (A) Bathymetric map of Drake Passage showing the annual mean position of the circumpolar fronts in blue (from N to S: SAF = Sub-Antarctic Front; PF = Polar Front; SACCF = Southern Antarctic Circumpolar Current Front; SB = Southern Boundary of the ACC) (Orsi et al., 1995), core sites and location of flow speed profile shown in Fig. 1B (dotted red line); (B) Geostrophic flow velocities on transect through Drake Passage (Renault et al., 2011). Core positions have been projected onto this transect.

The top 50cm of GC528 (Holocene sediments) consist of foraminifera ooze containing >10% CaCO₃ and alkenone concentrations of >1 µg/g. The rest of the sequence is mainly composed of silt-bearing clay with occasional dropstones present (particularly towards the LGM). Weight percent carbonate is ~1% and the alkenone concentration is 0.5-1 µg/g.

The age model for core GC528 is based on reservoir-age corrected AMS ^{14}C dates on monospecific benthic foraminifera and has been described in full in Roberts et al. (2016). The sedimentation rate varies from 7 cm/kyr in the Holocene to 50 cm/kyr during the glacial.

2.2 Methods

2.2.1 Sortable silt grain size analysis

Sediment grain size distribution in the silt fraction (10-63 μm) is strongly controlled by the geostrophic speed occurring above the bottom mixed layer (McCave et al., 1995). A detailed grain size analysis of the silt fraction (with an average temporal resolution of 200 years), in which carbonate and biogenic silica had been removed (McCave et al., 1995), was performed using a Coulter Counter (Multisizer 3) (Bianchi et al., 1999) with a 200 μm aperture. The set-up was adapted following Moffa-Sanchez et al. (2015). The measurement error in the sortable silt mean grain size (\overline{SS}) was 0.48 μm (1 S.D., $n=8$).

2.2.2 Ice-rafted Debris

Counts of terrigenous grains $>300\text{ }\mu\text{m}$ (used as a proxy for coarse IRD) were made every 1cm in order to determine potential changes in the source of sediment and the effect on \overline{SS} . Ice-rafted debris comprises all grain sizes but we use counts of grains $>300\text{ }\mu\text{m}$ as a proxy for IRD because grains in this fraction are unlikely to be transported by other processes.

No obvious gravitational down-slope deposits were observed in the core, suggesting no influence from downslope transport that could have otherwise emplaced sediment unmodified by current transport at the site. Shards of Southern Andean volcanic ash or tephra have the potential to be transported significant distances by the south-westerly winds (SWWs), therefore grains of tephra were not counted.

2.2.3. Alkenone-derived Sea Surface Temperatures

Sea surface temperatures were calculated from the U_{37}^K index (Prahl et al., 1988) from alkenone analysis of core GC528 with an average sample resolution of 250 years. Lipids were extracted from $\sim 3\text{ g}$ of homogenised, freeze-dried sediment using a CEM microwave system with 12 mL of Dichloromethane (DCM):MeOH (3:1, v/v) (Kornilova and Rosell-Melé, 2003). Internal standards were added for quantification (5 α -cholestane, dotriacontane and tetracontane). The relative abundances of di-, tri-, and tetra-unsaturated C_{37} alkenones were measured with a Trace Ultra gas chromatograph directly coupled to a Thermo DSQ single quadrupole mass spectrometer, fitted with a programmed temperature vaporising (PTV) injector. The target m/z were: 300 (nonadecanone), 544 ($C_{37:4}$), 546 ($C_{37:3}$), 548 ($C_{37:2}$), 560 ($C_{38:3Et}$ and $C_{38:3Me}$), 562 ($C_{38:2Et}$ and $C_{38:2Me}$), 564 and 578 (C_{36}

alkyl alkenoates) (Rosell-Mele et al., 1995). Several samples were split and extracted separately to determine the procedural error of $U_{37}^K = \pm 0.034$ ($n = 12$; equating to an error in SST $\pm 1.2^\circ\text{C}$). The Prah et al., (1988) U_{37}^K -SST calibration produced the best match between the surface sample and modern annually-averaged sea surface temperatures at site GC528. This is because the Prah et al., (1988) calibration is based on the U_{37}^K index (as opposed to the $U_{37}^{K'}$), which includes $C_{37:4}$. This alkenone is abundant in high latitude regions and it has been shown that the U_{37}^K index provides more robust SST reconstructions in high Southern latitudes than $U_{37}^{K'}$ (Ho et al., 2012).

2.2.4. $\delta^{13}\text{C}_{\text{TOC}}$ and C/N ratio

Total organic carbon $\delta^{13}\text{C}_{\text{TOC}}$ and C/N ratio are used here to track changes in surface ocean productivity and organic carbon source. Decarbonated samples (at 5 cm resolution) were measured for organic carbon content following the method described in Könitzer et al., (2012). Percentage carbon and nitrogen and $\delta^{13}\text{C}_{\text{TOC}}$ analysis were performed by combustion on pre-weighed samples in an online system comprising a Costech ECS4010 elemental analyser (EA) coupled with a VG TripleTrap and a VG Optima dual-inlet mass spectrometer at the NERC Isotope Geosciences Laboratory. Each analytical run contained 10 replicates of the internal NIGL standard BROCC2 and 2 replicates of the external standard SOILB. $\delta^{13}\text{C}_{\text{TOC}}$ is reported relative to the VPDB standard, with a precision of 0.1‰ (1 S.D.).

2.3. Numerical Modelling

A numerical model is used to determine the effect of a change in sea level on bottom current flow speeds. The numerical model (Princeton Ocean Model, Blumberg and Mellor, 1987) is a regional nested implementation of the Regional Ocean Modeling System. At the base there is a parent model, which extends from 20°N to 70°S and from 180°E to 180°W with a horizontal resolution of $\frac{1}{4}^\circ$. The parent model is nudged to the monthly mean climatological values of Simple Ocean Data Assimilation (SODA) at its northern (open) boundary. Nested into this parent model there is a child model, which covers all the southwestern Atlantic and southeastern Pacific sectors with a horizontal resolution of $\frac{1}{12}^\circ$. The nested model configuration is forced with climatological mean wind stress forcing derived from the ERA-Interim data set. Surface heat and freshwater fluxes are derived from the COADS dataset. See Combes and Matano 2014 and Palma et al. 2008 for details.

An “LGM” sea level simulation was run such that the only difference from the control was a 120 m reduction in sea level. Note that this “LGM” simulation does not take into account topographic changes related to isostatic adjustment. The LGM and control simulations were spun-up to dynamical equilibrium and run in diagnostic mode for 5 model years. Average values of the last year of the diagnostic run are used in the present analysis.

3. Results

3.1 Grain size analysis

The \overline{SS} at site GC528 almost doubles across the last deglaciation, from a minimum of 18.2 μm at 19-18 ka to a maximum of 34.7 μm at 1 ka [Figure 2b]. There are two step-wise changes in \overline{SS} across the deglaciation; (i) between 21-19 ka, \overline{SS} decreases by 5.2 μm , (ii) between 14.5-14.0 ka, \overline{SS} increases by 5.0 μm . After 10 ka, there is a steady increase in \overline{SS} spanning the entirety of the Holocene.

There is a \overline{SS} -bottom current flow speed calibration for the Scotia – Weddell Sea region ($SS = 0.59U + 12.24$) based on six points for which the sensitivity is 1.69 $\text{cm s}^{-1}/\mu\text{m}$. However the greater confidence in the universal sensitivity of sortable silt mean grain size to bottom current flow speed based on 24 points of $1.47 \pm 0.20 \text{ cm s}^{-1}/\mu\text{m}$ (by Coulter Counter) (McCave et al., submitted) is preferred. The total deglacial change in \overline{SS} of 16.5 μm (34.7-18.2 μm) implies a change in bottom current flow speeds of 19.8-26.4 cm s^{-1} . Given that the largest grains in the silt size fraction (60 μm) transition into an erosion regime in flow velocities greater than 25 cm s^{-1} , the magnitude of this deglacial change in \overline{SS} must correspond to an increase in bottom current velocity from $<5 \text{ cm s}^{-1}$ to $\sim 20 \text{ cm s}^{-1}$ (using the lower limit of sensitivity).

3.2 Fidelity of \overline{SS} as record of bottom water flow

Several processes act on glacial-interglacial timescales that could affect the sedimentation at GC528, such as changes in flow strength, sea level and ice-rafting, which we discuss here.

Reconstruction of the LGM Patagonian coastline (based on modern bathymetry) places it 200 km closer to GC528 than it is today (Figure S1), potentially increasing sediment supply. This could impact on the reliability of \overline{SS} as a bottom current flow speed proxy if the rate of direct sediment introduction was faster than the current could rework. The sediment mass accumulation rate at GC528 was higher during the LGM than the Holocene (Figure S1b), likely reflecting a closer sediment source during glacial times as a result of the sea level lowstand. However, it is interesting to note that the mass accumulation rate at GC528 does not decrease linearly with increasing sea level across the deglaciation, suggesting that any relationship between sea level and sediment supply to GC528 is not straightforward. Increased rates of sea level rise at 20-19 ka and 14.5-13 ka coincide with elevated accumulation rates at GC528 (Figure S1b-c), perhaps suggesting that the initial flooding of exposed shelf may have affected sediment supply to the slope.

At high latitudes, ice-rafted sediment provides additional material to the core site with significant fluctuations on glacial-interglacial timescales. At site GC528, high concentrations of IRD are observed

during the LGM [Figure 2c]. This is consistent with acoustic images of scours on the seafloor in the region suggesting the presence of icebergs in the past (Brown et al., 2017). The concentration of IRD at GC528 rapidly decreases between 20-19 ka, corresponding to a decrease in \overline{SS} (Figure S2b).

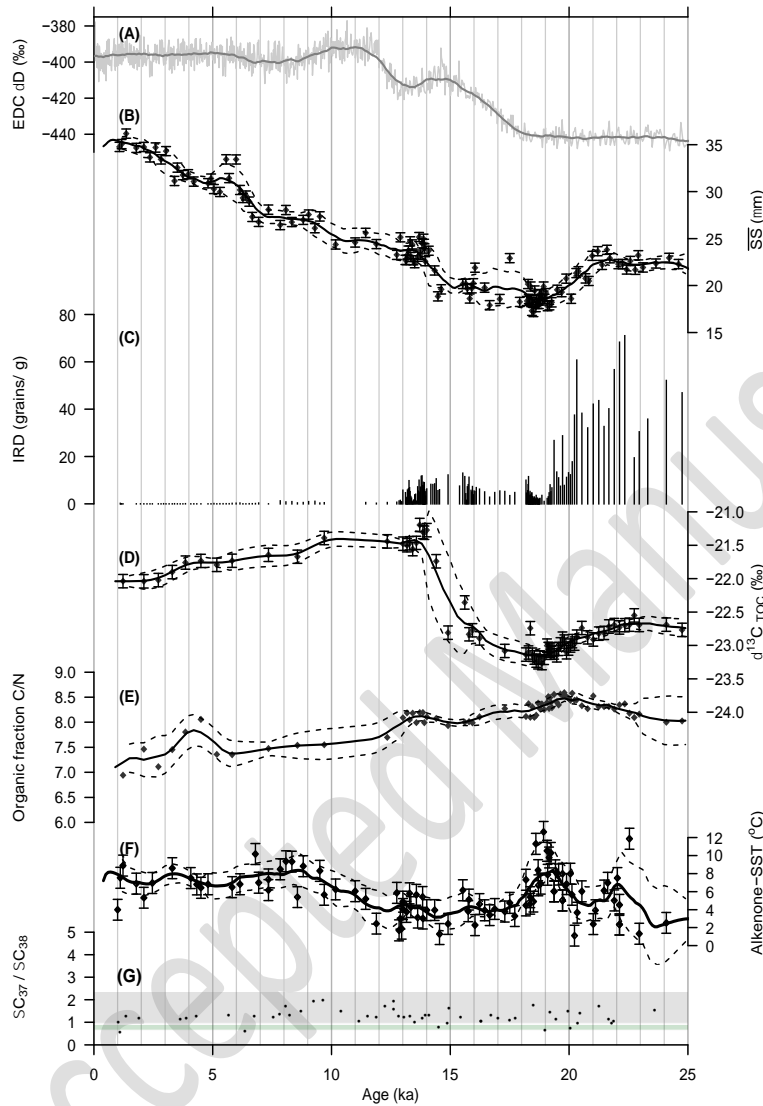


Figure 2: Deglacial grain size analysis, organic carbon and biomarker records from site GC528 in the southwest Atlantic. (A) EPICA Dome C (EDC) δD record on the AICC2012 age scale (Veres et al., 2013); (B) Mean sortable silt grain size (\overline{SS}); (C) Counts of grains $>300 \mu m$, used as a proxy for IRD; (D) Total organic carbon (TOC) $\delta^{13}C$; (E) Organic carbon C/N ratio; (F) Alkenone-derived SST based on the U_{37}^k index (Prahl et al., 1988); (G) Total $C_{37}:C_{38}$ alkenones used here to track changes in the alkenone-producing community. Grey and green bars show the typical range of *E.huxleyi* and *G.oceanica* $C_{37}:C_{38}$ ratio based on culture studies (Volkman et al., 1995). In each record, the 2σ analytical precision is shown by the error bars, and a 1500 yr moving average and 1σ moving standard deviation of each record is shown by the solid line and dashed lines respectively.

Do the variations in the sedimentation rate across the last deglaciation reduce confidence in \overline{SS} as an indicator of bottom current flow speed? The key assumption underlying the \overline{SS} proxy is that the sediment must be current sorted (McCave et al., 1995). Lamy et al., (2015) used the correlation between \overline{SS} and %SS to demonstrate current sorting at sites within the Drake Passage. In GC528, the cross-plot of \overline{SS} and %SS (measured on a subset of the samples, with a temporal resolution of 500 years) reveal that the sortable silt fraction of all sediments within GC528 has been current sorted, even within intervals that have been strongly influenced by IRD (Figure S2a), and there is no correlation between \overline{SS} and IRD concentration (Figure S2b). Therefore, we are confident that the \overline{SS} presented here can be interpreted as a reliable record of bottom current flow speeds.

3.3 Source of IRD in the southwest Atlantic

Variations in IRD concentrations occur across the last deglaciation at site GC528 (Figure 2c). The two most significant potential source regions of this IRD are Patagonia and Antarctica. Acoustic imaging of the shelf sediments north of the Falkland islands have identified iceberg scours at present-day water depths of 240-480m (Brown et al., 2017). These authors argue that the depth of these scours requires large icebergs that could only have been derived from Antarctica. The anti-clockwise nature of the Antarctic coastal current means that icebergs calving off Antarctic glaciers typically accumulate within the Weddell Sea (Stuart and Long, 2011). From the Weddell Sea, most of the Antarctic icebergs escape into the ACC via “Iceberg Alley”. Weber et al. (2014) identified several large iceberg discharge events from the Weddell Sea during the last deglaciation. However, consistent with icebergs drifting eastwards with the ACC from the Scotia Sea region, the timing of these iceberg discharge events (18-12 ka) do not coincide with the maximum IRD concentration at site GC528 (21-19 ka) (Figure S3), indicating that the source of IRD at GC528 was distinct from the Scotia Sea. We consider it likely that the dominant source of IRD deposited at GC528 was derived from marine-terminating glaciers on the west coast of Patagonia and transported through the Drake Passage. However, an exclusively Patagonian origin of IRD in this region is inconsistent with the inference of Brown et al. (2017) based on iceberg size, suggesting that icebergs sourced from East Antarctic may also have approached our site via the Drake Passage. A detailed IRD provenance study would be required to further test this hypothesis.

3.3 Productivity changes at site GC528

The $\delta^{13}C_{TOC}$ reflects variations in both surface water productivity and source of organic matter, whereas the C/N ratio is primarily driven by the organic carbon source. In core GC528, organic carbon $\delta^{13}C_{TOC}$ increases from values ranging between -23.0 to -22.6 ‰ prior to 15 ka, to -21.5 to -21.0 ‰ after 14 ka [Figure 2d]. In contrast the C/N ratio gradually decreases across the deglaciation

and Holocene with no marked shift in the C/N ratio at 15-14 ka [Figure 2e]. Taken together, we suggest the shift at 15-14 ka to more positive $\delta^{13}\text{C}_{\text{TOC}}$ reflects a change in surface ocean productivity.

3.4 Alkenone-derived SST

Alkenone-derived SST across the last deglaciation is highly variable [Figure 2e]. The Holocene (10-0 ka) average SST (7.6 ± 2.0 °C) is in good agreement with modern annual average SSTs at the core location. In contrast to other southern hemisphere alkenone records (e.g. Caniupán et al., 2011; Kaiser et al., 2005), the LGM (19-22 ka) average alkenone-derived SST at GC528 is relatively warm (7.0 ± 3.9 °C). However, this average value masks the large fluctuations that are apparent in the alkenone-SST record across the LGM. The LGM SSTs fluctuate between a minimum of 1.3°C at 25-23 ka and a maximum of 8°C at 19 ka, and there are two intervals spanning the end of the last glacial period (20-18.5 ka and 23-22 ka) during which SSTs in the southwest Atlantic were elevated by 4-6°C above the glacial mean. Replicate analyses on samples over this interval confirm that these warm LGM temperature signals are robust. In the following, we evaluate factors that may result in the elevated LGM alkenone-derived SSTs.

3.5 Fidelity of alkenone- U_{37}^{K} as record of sea surface temperature

Variations in the dominant alkenone-producing haptophyte could require the use of different regressions between U_{37}^{K} and SST. The abundance of ΣC_{37} : ΣC_{38} alkenones within a sediment sample has been used to identify shifts in the dominant alkenone-producing haptophyte population (McClymont et al., 2005). We identify no significant shift in the ΣC_{37} : ΣC_{38} ratio over the interval studied [Figure 2f] with values averaging 1.16, in the range of *Emiliania huxleyi* (0.91-2.26) rather than the other dominant alkenone-producing haptophyte *Gephyrocapsa oceanica* (0.59-0.81) (Volkman et al., 1995). This suggests that no change in the dominant alkenone producing haptophyte population occurred, and thus the U_{37}^{K} -SST relationship should have remained constant.

Preferential degradation of components with a greater degree of unsaturation may bias the alkenone-SST record towards warmer values (Flügge, 1997). We consider the percentage of the cold tetra-unsaturated $\text{C}_{37:4}$ alkenone that would need to be removed in order to produce LGM SSTs as low as during the late deglaciation period (2.2°C at 11.9 ka). We find that to account for a diagenetic bias of 6°C, at least 70% of the 'original' $\text{C}_{37:4}$ would have to be removed from the samples. Such a significant amount of alteration has not been observed experimentally or within sediments studied from this time period (Flügge, 1997).

Advection of warm water alkenones has been used to explain a warm LGM alkenone-SST signal in some regions of the ocean. Modern alkenone studies from sites influenced by the Falkland Current (Benthien and Müller, 2000) demonstrate that alkenone-derived SSTs from this region are biased

towards colder temperatures as a result of strong northward transport by the Falkland Current and deep western boundary current. However core-top alkenone-SST data from site GC528 (7.7 °C) shows good correlation with modern SSTs suggesting that advection does not strongly bias the alkenone-SST signal at this site.

Reworking of alkenones from older warm intervals (such as the Eemian) could overprint the original alkenone-SST and bias the alkenone signal to warmer temperatures. However, we do not believe this to be a significant issue at site GC528 because (i) neither the TOC or the alkenone concentrations during the two “warm” intervals during the LGM are significantly higher than the LGM average [Figure S3b-c], and (ii) other proxies such as planktonic $\delta^{18}\text{O}$ [Figure S3d] show no evidence of reworking. In addition, the spatial distribution of “warm” alkenone-derived LGM SST records is globally distributed (Barrows et al., 2011). If all the sites were influenced by older reworked alkenones, they would all have to be simultaneously affected by (specifically warm) reworked alkenones during the LGM only. This seems an improbable explanation.

Changes in the seasonality of alkenone production can affect the temperatures recorded by the alkenones. In high latitude regions, the limitation of light and the extreme surface conditions restrict alkenone production to a short summer growth season (Ternois et al., 2000). Site GC528 is located in the sub-Antarctic, and is sufficiently far north that it is not light limited. However, could there be other processes in play during the LGM that affects the seasonality of alkenone production? Whilst it is unlikely that sea ice was able to accumulate (even seasonally) across the Drake Passage, there exist very indirect arguments supporting the idea that sea ice may have been present between the Falkland Islands and Argentina during the LGM (Austin et al., 2013); however, we find no evidence of any sea ice biomarkers (i.e. highly-branching isoprenoids (Collins et al., 2013)) in the glacial samples of GC528. Alternatively, the accumulation of large icebergs in an “iceberg graveyard” around the Falkland shelf (Brown et al., 2017) could have generated shallow meltwater stratification in the surface ocean, potentially biasing summer SSTs (Peck et al., 2008). High IRD concentrations coincident with both apparent warming events lend weight to this hypothesis [Figure 2c].

Despite our concern that seasonality could have led to a warm bias in the glacial alkenone SST at site GC528, a global comparison of seasonality in alkenone flux demonstrated that at a global scale, the mean annual SST signal still dominates the sedimentary record (Rosell-Melé and Prahl, 2013). Furthermore, where high latitude seasonality in alkenone production has been shown (Conte et al., 2006), the bias relative to the expected mean annual SST was only 2.5°C. Subtracting this value from our glacial-stage warm intervals does not compensate the 4 °C anomalies relative to the other samples; thus, the intervals of warming remain. As we show later (Section 4.1), seemingly logical spatial trends in SSTs can be inferred from the comparison of this SST record with other alkenone-

SST records in the Drake Passage region (see Section 4.1). We therefore argue that whilst a seasonality overprint of the glacial alkenone-SST record could have contributed to the magnitude of the warmings, the overall pattern in SSTs remains robust.

4. Discussion

4.1 The 15-14 ka event

The \overline{SS} record from site GC528 shows a step-wise increase in bottom current flow speeds ($\Delta U = 6.4 \text{ cm s}^{-1}$) at 14.5-14 ka [Figure 2b]. Coupled with the change in bottom current velocity, there is evidence of a significant increase in $\delta^{13}\text{C}_{\text{TOC}}$ [Figure 2d], potentially reflecting increased surface ocean productivity. Today, the Falkland Current (the most northerly ACC jet associated with the SAF) acts as the primary source of nutrients to the surface ocean above site GC528, supporting high concentrations of chlorophyll along the shelf break. While the Falkland Current remains in-situ, surface productivity is relatively unresponsive to changes in dust flux (unlike other sub-Antarctic sites). This idea is supported by our record of $\delta^{13}\text{C}_{\text{TOC}}$, which shows little response to the well-known decrease in dust between 18-17 ka (Lambert et al., 2008). This indicates that the prominent increase in $\delta^{13}\text{C}_{\text{TOC}}$ at 14.5-14 ka was likely driven by reorganisation of the oceanic currents in the region. Oceanic current reorganisation would impact the supply of nutrients and/or the thermohaline properties of the surface ocean, affecting surface productivity. Furthermore, reorganisation would impact the bottom current speeds, so would be expressed in the \overline{SS} record.

Understanding the nature of the inferred change in ocean circulation at 14.5-14 ka requires comparison with other sites in the region. Site MR806-PC9 is located at the northern margin of the Drake Passage [Figure 1a], and is today immediately upstream of site GC528 within the jet associated with the SAF [Figure 1b]. Comparison of the \overline{SS} records between site GC528 and MR806-PC9 (Lamy et al., 2015) reveals a remarkable similarity in bottom current speed at the two sites between 14-0 ka [Figure 3b]. In contrast, prior to 14 ka, there was divergence between the two \overline{SS} records [Figure 3b], with faster bottom current flow speeds in Drake Passage than on the South Falkland slope.

The fact that sites GC528 and MR806-PC9 presently lie within the core of the main SAF jet [Figure 1b] and have similar bottom current flow speeds over 14-0 ka [Figure 3b] suggests a common response to changes in the intensity of the SAF jet. Both records suggest strengthening of the SAF jet through the Drake Passage over the late deglaciation and Holocene (which we discuss in Section 4.2). In contrast, the disparity in bottom current flow speeds prior to 14 ka - with faster flow speeds in Drake Passage relative to the downstream site - could be the product of one of two different scenarios; (i) a lower glacial sea level meant that the SAF did not cross the topographic high of the

North Scotia Ridge and thus site GC528 was 'shielded' from the influence of the SAF, or (ii) the Southern Ocean frontal system shifted northwards relative to its current position such that the SAF did not extend through Drake Passage but instead was truncated by South America, analogous to the present Sub-Tropical Front. The faster flow speed at MR806-PC9 may then be the result of proximity to a more northerly position of the Polar Front.

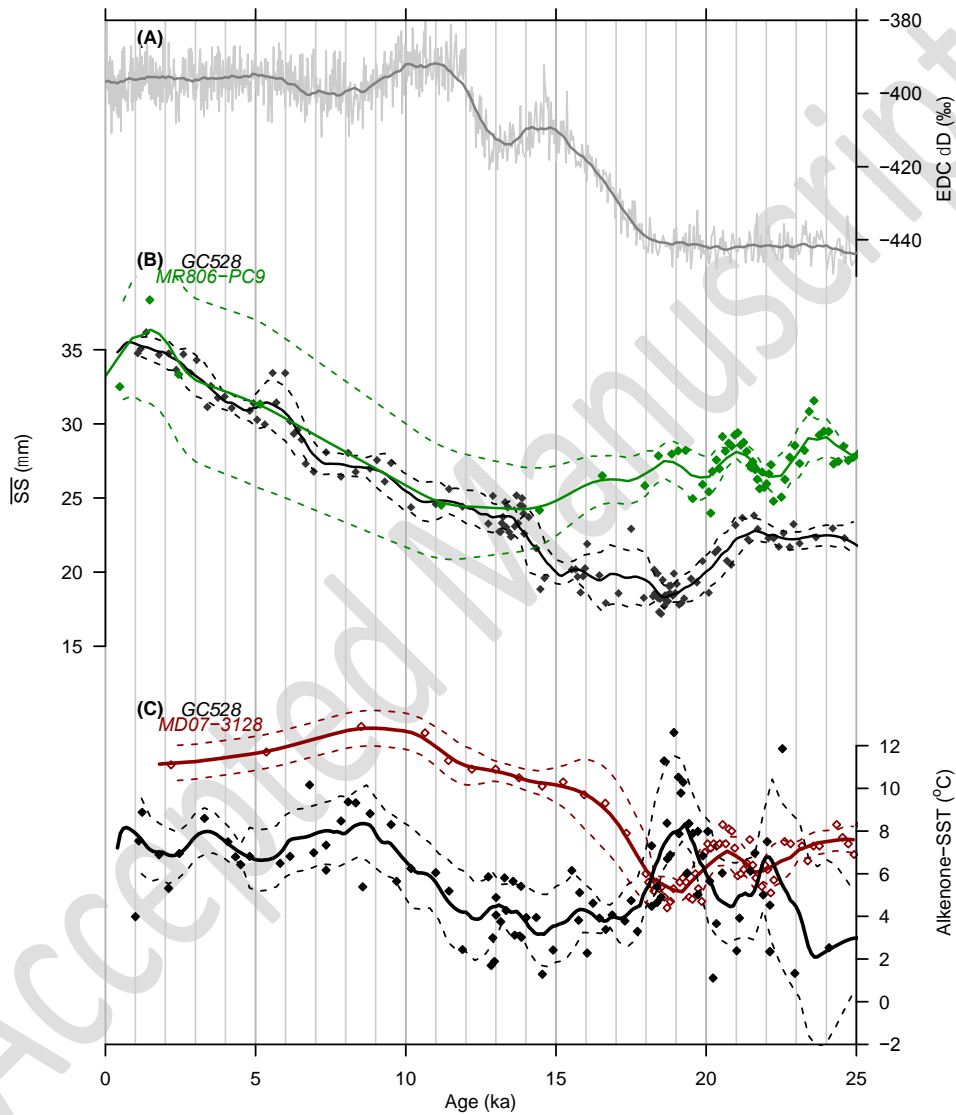


Figure 3: Comparison of proxy records from GC528 with upstream sites. (A) EPICA Dome C (EDC) δD record on the AICC2012 age scale (Veres et al., 2013); (B) Mean sortable silt grain size (\overline{SS}), GC528 (black) and MR806-PC9 (green; Lamy et al., 2015); (C) Alkenone-derived SST records from upstream (MD07-3128 - red, Caniupán et al. 2011) and downstream (GC528 - black) of the Drake Passage. A 1500 yr moving average and 1 σ moving standard deviation of each record is shown by the solid line and dashed lines respectively.

In order to test Scenario 1 (a lower sea level shielded GC528 from the SAF), we modelled the effect of a lower sea level on bottom current flow speeds. The model predicts an overall increase in bottom current flow within the Drake Passage [Figure 4]. This increase is because the ACC is an equivalent barotropic jet and therefore, bottom current velocities are inversely proportional to the depth of the fluid. In contrast to the general strengthening within the Drake Passage, the model predicts a decrease in bottom current flow speeds of 10-15 cm s^{-1} at site MR806-PC9 [Figure 4].

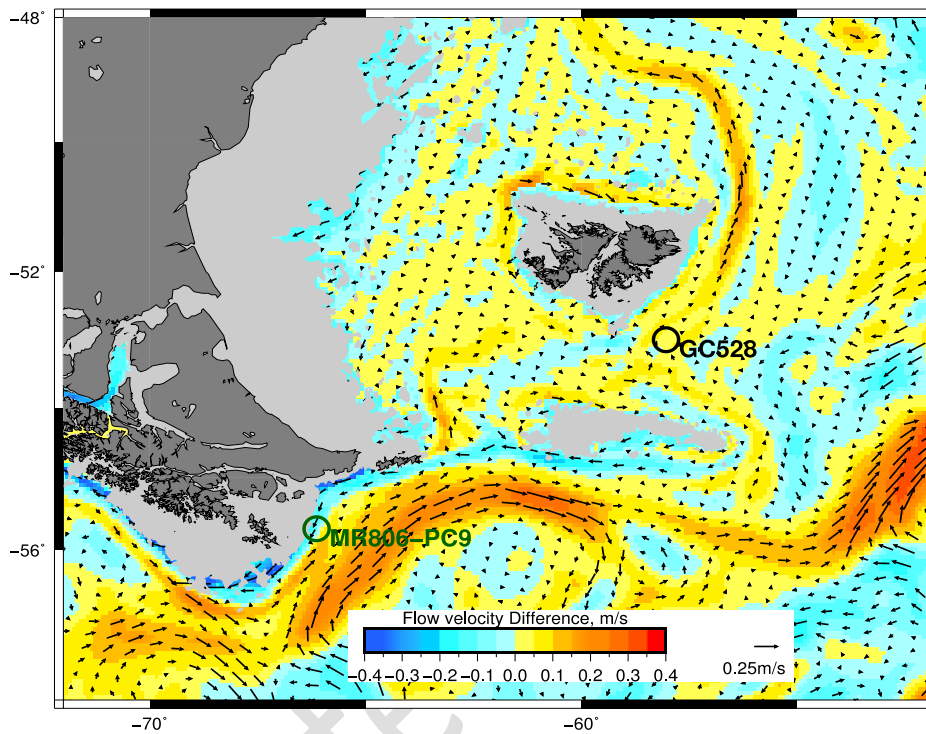


Figure 4: Model simulations of changes in bottom water flow speeds as a result of a lowering of sea level. Plot shows the relative change in bottom current flow velocity as a result of a -120m reduction in sea level. A reduction in bottom current velocity is highlighted by the blue colours. Green and black open circles show the position of MR806-PC9 (in Drake Passage) and GC528 (south of the Falkland Islands) respectively. Pale grey shows the model coastline in the low sea level scenario.

This is driven by the development of a frictional recirculation cell that occupies the space between the continent and the intensified offshore flow, and is highly dependent on the model configuration, and is therefore not a robust prediction. At site GC528, the model predicts an increase of 6 cm s^{-1} in northward advection of bottom water during sea level lowstands [Figure 4]. This predicted increase in transport at GC528 is driven by a reduction in on-shelf transport, resulting in an increase in transport along the shelf-break. Because the Patagonian shelf is so expansive, a reduction in sea level results in a large reduction in on-shelf transport (and subsequent increase in shelf-break

transport) relative to the minor reduction in the transport across the North Scotia Ridge. Therefore a relative strengthening of bottom currents is predicted at GC528. The model predictions are inconsistent with our \overline{SS} reconstructions across the 15-14 ka transition, which suggest a significantly weaker bottom current before 15 ka at site GC528 and a stronger bottom water flow at MR806-PC9. Whilst we emphasise the uncertainty in the model prediction at MR806-PC9, we are confident in the model result at GC528. The discrepancy between the model prediction and the \overline{SS} reconstructions implies that sea level change is not the driver of the change in bottom current flow speeds observed in the records at GC528 (and possibly also MR806-PC9). Instead, oceanographic changes other than eustatic sea level change must have controlled the observed bottom current speed changes.

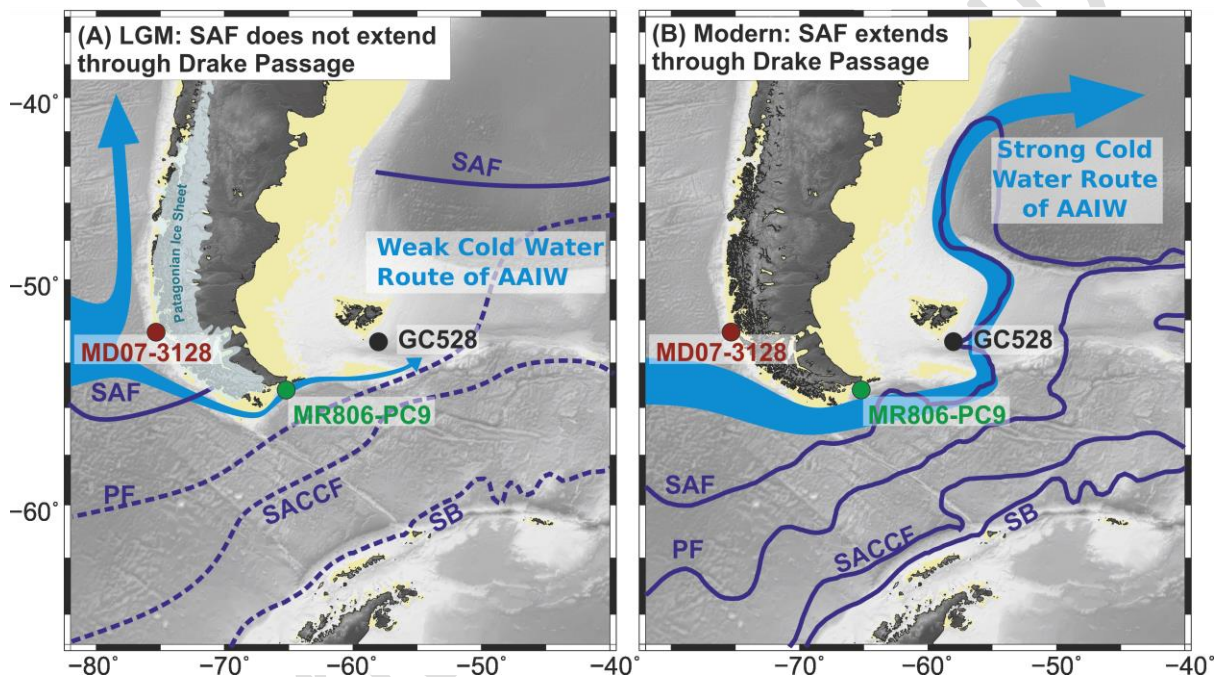


Figure 5: Schematic of changes in ACC frontal jets from the last glacial period to the Holocene with inferred inter-basinal exchange between Pacific and Atlantic. (A) Glacial ACC flow showing SAF located northwards of its present position and little inter-basinal exchange; (B) Holocene ACC flow showing the SAF extending through the Drake Passage and enhanced inter-basinal exchange. The positions of the ACC fronts are shown by the blue lines (more speculative locations denoted by dashed lines). The “Cold Water Route” water shown by light blue arrow. SAF = Sub-Antarctic Front; PF = Polar Front; SACCF = Southern Antarctic Circumpolar Current Front; SB = Southern Boundary Front.

An alternative hypothesis invokes a change in the position of the oceanic fronts. LGM front reconstructions (e.g. Gersonde et al., 2005) suggest that the Southern Ocean fronts were located 5-10° northward of their present position. We propose that during the last glacial and early deglacial period (until 15 ka), the SAF did not extend through the Drake Passage but was instead truncated by

the South American continent (similar to the modern Sub-Tropical Front; Figure 5a). If the SAF did not extend through the Drake Passage, slower bottom current flow velocities at both GC528 and MR806-PC9 would be expected. The fact that bottom current flow speeds at MR806-PC9 are significantly faster than GC528 prior to 15 ka [Figure 4b] suggests that this is not the entire story, and may be influenced by a more northerly located Polar Front [Figure 5a] or a decrease in sea level (given the model uncertainty at this location).

Support for the idea of a northward shifted SAF can be found in the Pacific-Atlantic SST phase relationships over the last deglaciation. The comparison of alkenone-SST records from GC528 and two sites upstream of the Drake Passage [Figure 1a], site MD07-3128 (Caniupán et al., 2011) and ODP 1233 (Kaiser et al., 2005) reveals a striking SST anti-correlation prior to 15 ka [Figures 3c, 6c]. Intervals of warming downstream of the Drake Passage (e.g. 23-22 ka and 20-18 ka) coincide with significant cooling upstream. From 14 ka onwards, this anti-phase relationship is absent [Figures 3c, 6b]. In contrast, planktonic Mg/Ca-derived SSTs downstream of GC528, at the Brazil Margin site GL-1090 (24°S, 42°W; Santos et al., 2017) are in-phase with site GC528 throughout the last deglaciation [Figure 6]. The idea of a “thermal see-saw” between the southeast Pacific and the southwest Atlantic

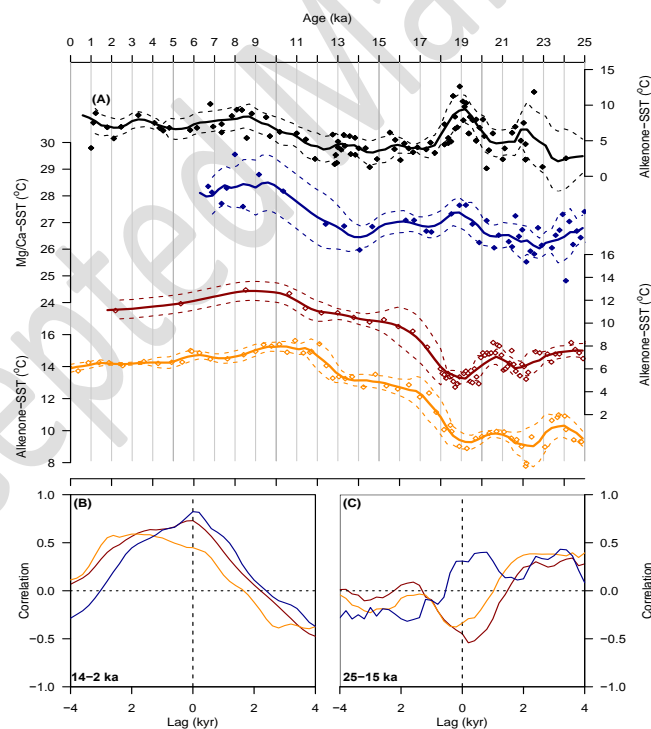


Figure 6. (A) Sea surface temperature records from GC528 (black) and GL-1090 (blue, Santos et al., 2017) from the southwest Atlantic, and sites MD07-3128 (red, Caniupán et al., 2011) and 1233 (orange, Kaiser et al., 2005) from the Chile Margin. (B) Cross-correlation between GC528 and MD07-3128 (red), GC528 and 1233 (orange), and GC528 and GL-1090 (blue) for the interval 14-2 ka; (C) Cross correlation for 25-15 ka, colours as in (B).

during the last glacial and early deglacial period (25-15 ka) supports the inference of northward shifted SAF during the LGM and early deglaciation. In the southeast Pacific, SSTs are controlled by the balance between cold sub-Antarctic Surface Water of the ACC advected northeastwards and warm surface waters transported southwards by the Chilean Coastal Current (Strub et al., 1998). Similarly, the SSTs in the southwest Atlantic represent a balance between cold southern-sourced water transported through the Drake Passage (Talley, 1999) and warm northern-sourced water carried southwards via the Brazil Current (Peterson and Stramma, 1991). Hypothesising that the SAF was absent from the Drake Passage during the LGM, a significant proportion of the cold water transported via the ACC to the Chilean margin would be redirected northwards into the Pacific (Lamy et al., 2015). This results in a relative cooling in the southeast Pacific and warming in the southwest Atlantic [Figure 5a]. Note that, based on our hypothesis, we argue that the warm LGM SST records from the Brazil Margin (Santos et al., 2017) are the result of a reduction in cold water advected through the Drake Passage, rather than an increase in warm water advected south from the Equator. The transition to in-phase SSTs upstream and downstream of Drake Passage at ~14 ka is consistent with the southward migration of the SAF to pass through the Drake Passage [Figure 5b]. A southward shift of the SAF would increase the inter-basin exchange of water between the Pacific and Atlantic, enabling temperature perturbations upstream of Drake Passage to be propagated rapidly to regions downstream of this gateway.

In summary, sortable silt, SST and $\delta^{13}\text{C}_{\text{TOC}}$ records from GC528 suggest a significant change in ocean circulation in the southwest Atlantic at 15-14 ka. Comparison of bottom current flow speeds downstream and within the Drake Passage provides evidence for a significant reorganisation of the frontal structure in the Drake Passage region across this interval. In particular, we suggest that the SAF did not extend through the Drake Passage until 15-14 ka. Anti-phased alkenone-SST records upstream and downstream of the Drake Passage support the idea of a reduced inter-basinal connection prior to 15 ka.

4.2 Strengthening of flow in the SAF after 14 ka

Bottom current flow speeds downstream (GC528) and within the Drake Passage (MR806-PC9) evidence a significant increase ($\overline{\Delta SS}$ of $11.5 \mu\text{m}$ suggests an increase of $\sim 16 \text{ cm s}^{-1}$) since 14 ka. Given that both sites record a very similar \overline{SS} record throughout this period, we infer that both sites are responding to an in-situ increase in the strength of the jet associated with the SAF. A strengthening of the SAF is supported by ϵNd records from the Brazil Margin (Howe et al., 2016), which show increasingly radiogenic Nd isotopic signatures across the Holocene, indicating a greater through-flow of Pacific-derived AAIW.

The cause of such a large increase in the strength of the SAF jet is difficult to determine. The density difference either side of a front results in a strong pressure gradient, which is balanced by the Coriolis force producing a strong eastward jet. At a basic level, a stronger density gradient across a front will strengthen the associated jet (Thompson, 2008). The SAF is the location where cold-fresh dense Antarctic-derived water subducts beneath less dense water to the north to form Antarctic Intermediate Water (Hartin et al., 2011). The increase in the strength of the jet associated with the SAF may thus be the result of an increase in the density contrast between sub-Antarctic Surface Water north of the SAF and Antarctic surface waters south of the SAF.

Proxy data of SSTs from north and south of the SAF do not provide strong support for the idea of an increased north-south temperature-driven surface density gradient during the Holocene. Sea surface temperature records of Antarctic surface water across the Holocene in the South Atlantic (Figure 7D; Nielsen et al., 2004) suggest an early Holocene warming followed by a cooler interval between 7-4 ka, and a relative warming from 4 ka to the present. In contrast, SST records north of the SAF from the Chilean margin suggest an initial warming in the Early Holocene followed by a general cooling trend (Figure 7C; Kaiser et al., 2005). Over the course of the Holocene, there is significant fluctuation in the north-south SST gradient; however, the long-term Holocene trend suggests a general decrease in the SST gradient [Figure 7E]. Based on this evidence, we cannot attribute the increase in the intensity of the SAF jet to an increase in a density gradient driven by temperature across the front. Note that the sites that we have used to reconstruct the SST gradient in Figure 7 are not proximal to the SAF and so may not accurately reflect SST gradients in the vicinity of the SAF. Alternatively, there remains the possibility of salinity-driven changes related to ice-melt, but we have no data to examine this aspect, nor (to our knowledge) are there any proxy data reconstructions of salinity across the SAF. However, it should be noted that the melt-related salinity gradients in the Southern Ocean were probably at a maximum during the deglaciation (18-12 ka) when the majority of ice was lost from Antarctica and Patagonia, and not during the Holocene.

Finally, based on current understanding of the ACC, we observe that it is difficult to determine how changes in the intensity or position of the south westerly winds (SWW) might drive changes in the strength of the SAF jet. The SWWs transfer momentum into the surface ocean of the ACC, which sets up the barotropic component of flow (e.g. Allison et al., 2010). However, the exact relationship between the overlying wind forcing and the response of the ACC remains a matter of debate and is model dependent (Hogg et al., 2008 and references therein). Eddy compensation and eddy saturation result in non-linear responses of the ACC to changes in wind forcing, and jets are a finer scale that is not often well resolved in models. Furthermore, even if the response of the ACC could be predicted, proxy reconstructions of SWW strength show that the SWWs did not increase

monotonically across the Holocene (Lamy et al., 2010). On balance, wind stress cannot adequately explain the seemingly linear increase in bottom current flow speeds suggested by data presented here

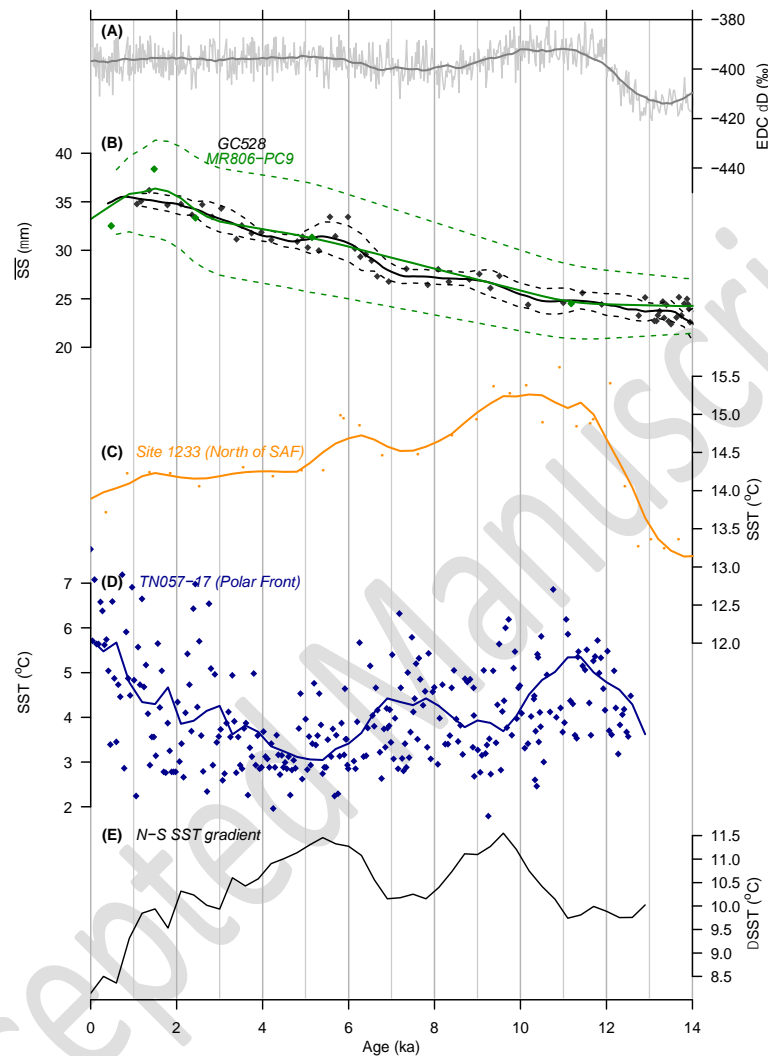


Figure 7: Reconciling the increase in strength of the SAF with changes in SST gradients over the Holocene. (A) EPICA Dome C (EDC) δD record on the AICC2012 age scale (Veres et al., 2013); (B) Mean sortable silt grain size, GC528 (black) and MR806-PC9 (green; Lamy et al., 2015); (C) Alkenone-SST record from the Chilean Margin, north of the SAF (orange; ODP site 1233, Kaiser et al., 2005); (D) Diatom transfer function based SST reconstruction from the Atlantic Sector of the Southern Ocean, at the Polar Front (blue; Core TN057-17, Nielsen et al., 2004); (E) Difference between the two SST records (C and D), used here as an indication of the density gradient across the SAF. A 1500 yr moving average and 1σ moving standard deviation of each record is shown by the solid line and dashed lines respectively.

In summary, the increase in bottom current velocities at sites in the Drake Passage and on the South Falkland slope since 14 ka suggests an increase in the strength of the SAF jet. However, the underlying cause of the increase in SAF jet strength remains enigmatic. Improved knowledge of sea surface salinity and temperature in the Drake Passage region could provide a key to understanding the increase in SAF jet flow speed across the Holocene.

4.3 Implications for the Atlantic Meridional Overturning Circulation (AMOC)

A key idea presented here is that of a thermal seesaw between the southeast Pacific and southwest Atlantic during the last glacial period and early deglacial (25-15 ka). This, we argue, was related to a reduction in the interbasinal connection via the Drake Passage as a result of a northward shifted SAF. The following discussion concerns the wider effect of these changes on ocean circulation.

The relative proportion of water flowing into the Atlantic basin via the Cold and Warm Water Routes affects the thermohaline properties of the shallow northward return flow. Extension of the SAF through the Drake Passage would have transmitted a greater volume of cold SAMW into the southwest Atlantic via Drake Passage, with potential consequences for global ocean circulation.

The onset of the southward shift of the SAF at 15-14 ka is synchronous with a 'spin-up' of the AMOC during the Bølling-Allerød interstadial (McManus et al., 2004; Skinner et al., 2013). This AMOC spin-up has commonly been interpreted to reflect changes in North Atlantic freshwater forcing, but the flow of water through the Drake Passage might also have played a role. Reduced throughput of cold low-salinity SAMW during the LGM would result in denser Atlantic AAIW (relative to today). If the density of Atlantic AAIW advected into the North Atlantic exceeds the density of NADW, then AMOC is potentially unstable (Keeling and Stephens, 2001). In contrast, a southward shift of the SAF at 15-14 ka would increase the transport of low-salinity SAMW into the Atlantic and decrease the density of AAIW relative to NADW, producing a more stable AMOC (Keeling and Stephens, 2001), and could explain the re-invigoration in AMOC observed during the Bølling-Allerød interstadial (McManus et al., 2004; Skinner et al., 2013). Support for this hypothesis comes from modelling studies (Weaver et al., 2003) which show that, given an initial circulation state in which the density of AAIW is greater than that of NADW, it is possible to spin up AMOC circulation by freshening AAIW in the vicinity of the Drake Passage. In this scenario, Drake Passage through-flow would act as a driver of AMOC circulation.

5. Conclusion

In this study, detailed grain size data and SST records from sites along the northern margin of Drake Passage were used to determine changes in the flow and frontal structures within the Drake Passage

since the LGM. In particular, we focus on the interval between 15-14 ka when an increase in bottom water current speeds is accompanied by increased in $\delta^{13}\text{C}_{\text{TOC}}$ in the southwest Atlantic, indicating significant reorganisation of the currents. Comparison of bottom current flow speeds in the southwest Atlantic under the influence of the SAF jet to an upstream site in the Drake Passage reveals very similar trends after 14 ka, indicating that both sites are responding to changes in the strength of the SAF jet. In contrast, prior to 15 ka, bottom current speeds at the two sites are dissimilar. We propose that during the interval prior to 15 ka, the SAF did not extend through Drake Passage but instead lay further north and was truncated by South America, similar to the modern STF. This hypothesis is supported by alkenone-based SSTs upstream and downstream of the Drake Passage that suggest through-flow via the Cold Water Route during the last glacial was reduced relative to today. We suggest that this reduction in the inflow of low-density SAMW during the LGM potentially had wider reaching implication for AMOC; the higher density of Atlantic AAIW relative to NADW may have contributed to a more sluggish overturning circulation in the Atlantic. In contrast, the subsequent southward migration of the SAF at 15-14 ka enabled a greater through-flow of low-density SAMW into the Atlantic, reducing the density of Atlantic AAIW and potentially contributing to the spin-up of AMOC during the Bølling-Allerød interstadial. If correct, our findings have significant implications for the importance of the Drake Passage in controlling AMOC stability.

Acknowledgments

We are grateful to S.J.Crowhurst, M.West and A.Hayton for providing technical assistance, and to M.Meredith for discussion. J.R. was funded jointly by the British Geological Survey/British Antarctic Survey (Natural Environment Research Council) and the University of Cambridge. ELM acknowledges funding from the Philip Leverhulme Prize. We thank the captain and crew of the RRS *James Clark Ross* for facilitating the collection of the marine sediment cores used in this study. The data reported in this paper are archived at www.pangaea.de

542 References

- 543 Allison, L.C., Johnson, H.L., Marshall, D.P., Munday, D.R., 2010. Where do winds drive the Antarctic
544 Circumpolar Current? *Geophys. Res. Lett.* 37, n/a-n/a. doi:10.1029/2010GL043355
- 545 Austin, J.J., Soubrier, J., Prevosti, F.J., Prates, L., Trejo, V., Mena, F., Cooper, A., 2013. The origins of
546 the enigmatic Falkland Islands wolf. *Nat. Commun.* 4, 1552. doi:10.1038/ncomms2570
- 547 Barrows, T.T., Chen, M.-T., de Vernal, A., Eynaud, F., Hillaire-Marcel, C., Kiefer, T., Lee, K.E., Marret,
548 F., Henry, M., Juggins, S., Londeix, L., Mangin, S., Matthiessen, J., Radi, T., Rochon, A., Solignac,
549 S., Turon, J.-L., Waelbroeck, C., Weinelt, M., 2011. Various paleoclimate proxy parameters
550 compiled within the MARGO project. doi:10.1594/PANGAEA.760904
- 551 Benthien, A., Müller, P.J., 2000. Anomalous low alkenone temperatures caused by lateral particle
552 and sediment transport in the Malvinas Current region, western Argentine Basin. *Deep Sea Res.*
553 *Part I* 47, 2369–2393. doi:10.1016/S0967-0637(00)00030-3
- 554 Bianchi, G.G., Hall, I.R., McCave, I.N., Joseph, L., 1999. Measurement of the sortable silt current
555 speed proxy using the Sedigraph 5100 and Coulter Multisizer IIe: precision and accuracy.
556 *Sedimentology* 46, 1001–1014. doi:10.1046/j.1365-3091.1999.00256.x
- 557 Blumberg, A.F., Mellor, G.L., 1987. A description of a Three-Dimensional Coastal Ocean Circulation
558 Model, in: Heaps, N.S. (Ed.), *Three-Dimensional Coastal Ocean Models*, Coastal and Estuarine
559 Sciences. American Geophysical Union, Washington, D. C., pp. 1–16. doi:10.1029/CO004
- 560 Brown, C.S., Newton, A.M.W., Huuse, M., Buckley, F., 2017. Iceberg scours, pits, and pockmarks in
561 the North Falkland Basin. *Mar. Geol.* 386, 140–152. doi:10.1016/j.margeo.2017.03.001
- 562 Caniupán, M., Lamy, F., Lange, C.B., Kaiser, J., Arz, H., Kilian, R., Baeza Urrea, O., Aracena, C.,
563 Hebbeln, D., Kissel, C., Laj, C., Mollenhauer, G., Tiedemann, R., 2011. Millennial-scale sea
564 surface temperature and Patagonian Ice Sheet changes off southernmost Chile (53°S) over the
565 past 60 kyr. *Paleoceanography* 26, PA3221. doi:10.1029/2010PA002049
- 566 Collins, L.G., Allen, C.S., Pike, J., Hodgson, D.A., Weckström, K., Massé, G., 2013. Evaluating highly
567 branched isoprenoid (HBI) biomarkers as a novel Antarctic sea-ice proxy in deep ocean glacial
568 age sediments. *Quat. Sci. Rev.* 79, 87–98. doi:10.1016/j.quascirev.2013.02.004
- 569 Combes, V., Matano, R.P., 2014. A two-way nested simulation of the oceanic circulation in the
570 southwestern Atlantic. *J. Geophys. Res. Ocean.* 119, 731–756. doi:10.1002/2013JC009498
- 571 Conte, M.H., Sicre, M.-A., Röhlemann, C., Weber, J.C., Schulte, S., Schulz-Bull, D., Blanz, T., 2006.
572 Global temperature calibration of the alkenone unsaturation index (U^{K7}_{37}) in surface waters
573 and comparison with surface sediments. *Geochemistry, Geophys. Geosystems* 7, n/a-n/a.
574 doi:10.1029/2005GC001054
- 575 Flügge, A., 1997. Variabilität von ungesättigten C 37 Methylketonen (Alkenone) in
576 Sinkstoffallenmaterial der Norwegischen See und deren Abbildung in Oberflächensedimenten.
577 Univ zu Kiel, Kiel Ph.D. Dissertation.
- 578 Gersonde, R., Crosta, X., Abelmann, A., Armand, L., 2005. Sea-surface temperature and sea ice
579 distribution of the Southern Ocean at the EPILOG Last Glacial Maximum—a circum-Antarctic view
580 based on siliceous microfossil records. *Quat. Sci. Rev.* 24, 869–896.
581 doi:10.1016/j.quascirev.2004.07.015

582 Gordon, A.L., Weiss, R.F., Smethie, W.M., Warner, M.J., 1992. Thermocline and intermediate water
583 communication between the south Atlantic and Indian oceans. *J. Geophys. Res.* 97, 7223.
584 doi:10.1029/92JC00485

585 Hartin, C.A., Fine, R.A., Sloyan, B.M., Talley, L.D., Chereskin, T.K., Happell, J., 2011. Formation rates of
586 Subantarctic mode water and Antarctic intermediate water within the South Pacific. *Deep Sea*
587 *Res. Part I Oceanogr. Res. Pap.* 58, 524–534. doi:10.1016/j.dsr.2011.02.010

588 Ho, S.L., Mollenhauer, G., Lamy, F., Martínez-García, A., Mohtadi, M., Gersonde, R., Hebbeln, D.,
589 Nunez-Ricardo, S., Rosell-Melé, A., Tiedemann, R., 2012. Sea surface temperature variability in
590 the Pacific sector of the Southern Ocean over the past 700 kyr. *Paleoceanography* 27, n/a-n/a.
591 doi:10.1029/2012PA002317

592 Hogg, A.M.C., Meredith, M.P., Blundell, J.R., Wilson, C., Hogg, A.M.C., Meredith, M.P., Blundell, J.R.,
593 Wilson, C., 2008. Eddy Heat Flux in the Southern Ocean: Response to Variable Wind Forcing. *J.*
594 *Clim.* 21, 608–620. doi:10.1175/2007JCLI1925.1

595 Howe, J.N.W., Piotrowski, A.M., Oppo, D.W., Huang, K.-F., Mulitza, S., Chiessi, C.M., Blusztajn, J.,
596 2016. Antarctic intermediate water circulation in the South Atlantic over the past 25,000?years.
597 *Paleoceanography* 31, 1302–1314. doi:10.1002/2016PA002975

598 Kaiser, J., Lamy, F., Hebbeln, D., 2005. A 70-kyr sea surface temperature record off southern Chile
599 (Ocean Drilling Program Site 1233). *Paleoceanography* 20, n/a-n/a. doi:10.1029/2005PA001146

600 Keeling, R.F., Stephens, B.B., 2001. Antarctic sea ice and the control of Pleistocene climate instability.
601 *Paleoceanography* 16, 112–131. doi:10.1029/2000PA000529

602 Koenitz, D., White, N., McCave, I.N., Hobbs, R., 2008. Internal structure of a contourite drift
603 generated by the Antarctic Circumpolar Current. *Geochemistry, Geophys. Geosystems* 9, n/a-
604 n/a. doi:10.1029/2007GC001799

605 Könitzer, S.F., Leng, M.J., Davies, S.J., Stephenson, M.H., 2012. An assessment of geochemical
606 preparation methods prior to organic carbon concentration and carbon isotope ratio analyses
607 of fine-grained sedimentary rocks. *Geochemistry, Geophys. Geosystems* 13.
608 doi:10.1029/2012GC004094

609 Kornilova, O., Rosell-Melé, A., 2003. Application of microwave-assisted extraction to the analysis of
610 biomarker climate proxies in marine sediments. *Org. Geochem.* 34, 1517–1523.
611 doi:10.1016/S0146-6380(03)00155-4

612 Lambert, F., Delmonte, B., Petit, J.R., Bigler, M., Kaufmann, P.R., Hutterli, M.A., Stocker, T.F., Ruth,
613 U., Steffensen, J.P., Maggi, V., 2008. Dust-climate couplings over the past 800,000 years from
614 the EPICA Dome C ice core. *Nature* 452, 616–619. doi:10.1038/nature06763

615 Lamy, F., Arz, H.W., Kilian, R., Lange, C.B., Lembke-Jene, L., Wengler, M., Kaiser, J., Baeza-Urrea, O.,
616 Hall, I.R., Harada, N., Tiedemann, R., 2015. Glacial reduction and millennial-scale variations in
617 Drake Passage throughflow. *Proc. Natl. Acad. Sci. U. S. A.* 112, 13496–501.
618 doi:10.1073/pnas.1509203112

619 Lamy, F., Kilian, R., Arz, H.W., Francois, J.-P., Kaiser, J., Prange, M., Steinke, T., 2010. Holocene
620 changes in the position and intensity of the southern westerly wind belt. *Nat. Geosci.* 3, 695–
621 699. doi:10.1038/ngeo959

622 McCave, I.N., Crowhurst, S.J., Kuhn, G., Hillenbrand, C.-D., Meredith, M.P., 2014. Minimal change in
623 Antarctic Circumpolar Current flow speed between the last glacial and Holocene. *Nat. Geosci.* 7,
624 113–116. doi:10.1038/ngeo2037

625 McCave, I.N., Manighetti, B., Robinson, S.G., 1995. Sortable silt and fine sediment size/composition
626 slicing: Parameters for palaeocurrent speed and palaeoceanography. *Paleoceanography* 10,
627 593–610. doi:10.1029/94PA03039

628 McClymont, E.L., Rosell-Melé, A., Giraudeau, J., Pierre, C., Lloyd, J.M., 2005. Alkenone and coccolith
629 records of the mid-Pleistocene in the south-east Atlantic: Implications for the UK'37 index and
630 South African climate. *Quat. Sci. Rev.* 24, 1559–1572. doi:10.1016/j.quascirev.2004.06.024

631 McManus, J.F., Francois, R., Gherardi, J.-M., Keigwin, L.D., Brown-Leger, S., 2004. Collapse and rapid
632 resumption of Atlantic meridional circulation linked to deglacial climate changes. *Nature* 428,
633 834–837. doi:10.1038/nature02494

634 Moffa-Sanchez, P., Hall, I.R., Thornalley, D.J.R., Barker, S., Stewart, C., 2015. Changes in the strength
635 of the Nordic Seas Overflows over the past 3000 years. *Quat. Sci. Rev.* 123, 134–143.
636 doi:10.1016/j.quascirev.2015.06.007

637 Nielsen, S.H.H., Koç, N., Crosta, X., 2004. Holocene climate in the Atlantic sector of the Southern
638 Ocean: Controlled by insolation or oceanic circulation? *Geology* 32, 317. doi:10.1130/G20334.1

639 Orsi, A.H., Whitworth, T., Nowlin, W.D., 1995. On the meridional extent and fronts of the Antarctic
640 Circumpolar Current. *Deep Sea Res. Part I* 42, 641–673. doi:10.1016/0967-0637(95)00021-W

641 Palma, E.D., Matano, R.P., Piola, A.R., 2008. A numerical study of the Southwestern Atlantic Shelf
642 circulation: Stratified ocean response to local and offshore forcing. *J. Geophys. Res.* 113,
643 C11010. doi:10.1029/2007JC004720

644 Peck, V.L., Hall, I.R., Zahn, R., Elderfield, H., 2008. Millennial-scale surface and subsurface
645 paleothermometry from the northeast Atlantic, 55–8 ka BP. *Paleoceanography* 23, n/a–n/a.
646 doi:10.1029/2008PA001631

647 Peterson, R.G., Stramma, L., 1991. Upper-level circulation in the South Atlantic Ocean. *Prog.*
648 *Oceanogr.* 26, 1–73. doi:10.1016/0079-6611(91)90006-8

649 Poole, R., Tomczak, M., 1999. Optimum multiparameter analysis of the water mass structure in the
650 Atlantic Ocean thermocline. *Deep Sea Res. Part I Oceanogr. Res. Pap.* 46, 1895–1921.
651 doi:10.1016/S0967-0637(99)00025-4

652 Prahl, F.G., Muehlhausen, L.A., Zahnle, D.L., 1988. Further evaluation of long-chain alkenones as
653 indicators of paleoceanographic conditions. *Geochim. Cosmochim. Acta* 52, 2303–2310.
654 doi:10.1016/0016-7037(88)90132-9

655 Renault, A., Provost, C., Sennéchal, N., Barré, N., Kartavtseff, A., 2011. Two full-depth velocity
656 sections in the Drake Passage in 2006-Transport estimates. *Deep Sea Res. Part II* 58, 2572–2591.
657 doi:10.1016/j.dsr2.2011.01.004

658 Roberts, J., Gottschalk, J., Skinner, L.C., Peck, V.L., Kender, S., Elderfield, H., Waelbroeck, C., Vázquez
659 Riveiros, N., Hodell, D.A., 2016. Evolution of South Atlantic density and chemical stratification
660 across the last deglaciation. *Proc. Natl. Acad. Sci. U. S. A.* 113, 514–519.
661 doi:10.1073/pnas.1511252113

662 Rosell-Mele, A., Carter, J.F., Parry, A.T., Eglinton, G., 1995. Determination of the UK'37 index in
663 geological samples. *Anal. Chem.* 67, 1283–1289. doi:10.1021/ac00103a021

664 Rosell-Melé, A., Prah, F.G., 2013. Seasonality of UK'37 temperature estimates as inferred from
665 sediment trap data. *Quat. Sci. Rev.* 72, 128–136. doi:10.1016/j.quascirev.2013.04.017

666 Santos, T.P., Lessa, D.O., Venancio, I.M., Chiessi, C.M., Mulitza, S., Kuhnert, H., Govin, A., Machado,
667 T., Costa, K.B., Toledo, F., Dias, B.B., Albuquerque, A.L.S., 2017. Prolonged warming of the Brazil
668 Current precedes deglaciations, *Earth and Planetary Science Letters*.
669 doi:10.1016/j.epsl.2017.01.014

670 Skinner, L.C., Scrivner, A.E., Vance, D., Barker, S., Fallon, S., Waelbroeck, C., 2013. North Atlantic
671 versus Southern Ocean contributions to a deglacial surge in deep ocean ventilation. *Geology* 41,
672 667–670. doi:10.1130/G34133.1

673 Strub, P.T., Mesias, J.M., Montecino, V., Rutllant, J., Salinas, S., 1998. Coastal ocean circulation off
674 western South America, in: Robinson, A.R., Brink, K.H. (Eds.), *The Global Coastal Ocean:
675 Regional Studies and Syntheses*. Wiley, New York, pp. 273–314.

676 Stuart, K.M., Long, D.G., 2011. Tracking large tabular icebergs using the SeaWinds Ku-band
677 microwave scatterometer. *Deep Sea Res. Part II Top. Stud. Oceanogr.* 58, 1285–1300.
678 doi:10.1016/j.dsr2.2010.11.004

679 Talley, L.D., 1999. Some aspects of ocean heat transport by the shallow, intermediate and deep
680 overturning Circulations, in: Clark, P.U., Webb, R.S., Keigwin, L.D. (Eds.), *Mechanisms of Global
681 Climate Change at Millennial Time Scales*. American Geophysical Union, Washington, D. C., pp.
682 1–22.

683 Ternois, Y., Kawamura, K., Ohkouchi, N., Keigwin, L., 2000. Alkenone sea surface temperature in the
684 Okhotsk Sea for the last 15 kyr. *Geochem. J.* 34, 283–293. doi:10.2343/geochemj.34.283

685 Thompson, A.F., 2008. The atmospheric ocean: eddies and jets in the Antarctic Circumpolar Current.
686 *Philos. Trans. A. Math. Phys. Eng. Sci.* 366, 4529–41. doi:10.1098/rsta.2008.0196

687 Veres, D., Bazin, L., Landais, A., Toyé Mahamadou Kele, H., Lemieux-Dudon, B., Parrenin, F.,
688 Martinerie, P., Blayo, E., Blunier, T., Capron, E., Chappellaz, J., Rasmussen, S.O., Severi, M.,
689 Svensson, A., Vinther, B., Wolff, E.W., 2013. The Antarctic ice core chronology (AICC2012): an
690 optimized multi-parameter and multi-site dating approach for the last 120 thousand years.
691 *Clim. Past* 9, 1733–1748. doi:10.5194/cp-9-1733-2013

692 Volkman, J.K., Barrerr, S.M., Blackburn, S.I., Sikes, E.L., 1995. Alkenones in *Gephyrocapsa oceanica*:
693 Implications for studies of paleoclimate. *Geochim. Cosmochim. Acta* 59, 513–520.
694 doi:10.1016/0016-7037(95)00325-T

695 Weaver, A.J., Saenko, O.A., Clark, P.U., Mitrovica, J.X., 2003. Meltwater pulse 1A from Antarctica as a
696 trigger of the Bølling-Allerød warm interval. *Science* 299, 1709–13.
697 doi:10.1126/science.1081002

698 Weber, M.E., Clark, P.U., Kuhn, G., Timmermann, A., Spreng, D., Gladstone, R., Zhang, X., Lohmann,
699 G., Menviel, L., Chikamoto, M.O., Friedrich, T., Ohlwein, C., 2014. Millennial-scale variability in
700 Antarctic ice-sheet discharge during the last deglaciation. *Nature* 510, 134–8.
701 doi:10.1038/nature13397

703

704

Supporting Material

705

Understanding the sortable silt flow speed proxy in marine systems with varying supply

706

707

708

709

710

The sortable silt proxy is predicated upon the premise that the grain-size of deposited sediment at a point is primarily controlled by the short term (a few tens of years) time history of flow speeds at that point acting on a broad spectrum of fine sediment sizes delivered along the transport path. Control of deposition is expressed in the classical Krone equation (Einstein and Krone, 1962; Krone, 1962) for the selective deposition of fine suspended material. The amount deposited is given by:

711

$$\sum R_i t = \sum C_i w_{si} (1 - \tau_o / \tau_{di}) t$$

712

713

714

715

where R_i is the rate of deposition (dimensions mass/area.time; $ML^{-2}T^{-1}$), thus $\sum R_i t$ is (ML^{-2}), to be summed over i size fractions. The controls are; settling velocity w_{si} , critical depositional stress τ_{di} , boundary shear stress τ_o and the concentration C_i for each fraction according to the size distribution supplied in suspension from upstream.

716

717

718

719

720

721

722

723

724

725

This has been set out extensively in the publications of McCave, 2008, 2007; McCave et al., 1995; McCave and Hall, 2006. All the material that is considered in the analysis of the proxy is derived from terrestrial sources because care is taken to remove biogenic components (carbonate and silica) of marine origin. These sediments are delivered to the ocean beyond the shelf via a variety of routes, primarily by gravity flows (turbidity currents and debris flows) and shelf-edge resuspension/ spill-over, but also in a number of cases by aeolian fallout and via ice rafting in polar areas. Direct fluvial supply is rare, particularly at present under high sea-level stand. Even under glacially lowered sea-levels many deltas did not reach the shelf edge and many others debouched directly into the heads of submarine canyons, feeding turbidity currents which led into the deep sea (see reviews by e.g. McCave, 2002; Thomsen et al., 2002).

726

727

728

729

730

731

732

733

A test of whether sediments are current sorted or not is derived from cross-plots of \overline{SS} against $SS\%$. Under a current sorted regime, \overline{SS} correlates positively with $SS\%$, whereas unsorted sediments show no correlation. The latter case is evident in a fluvially-supplied lake (Gammon et al., 2017) or in the sediments from the Mississippi delta top (Xu et al., 2016) (Figure S5). In contrast, the marine sediment cores in the Drake Passage in Lamy et al., (2015) show a high degree of sediment sorting (Lamy et al., (2015), their Figure S3). Similarly, GC528 (presented in this study) shows a strong correlation between \overline{SS} and $SS\%$ (Figure S2a) suggesting that the sediment has been current sorted. Furthermore, even though there are high IRD concentrations in some intervals, there is no

correlation between IRD concentration and \overline{SS} (Figure S2b) and the samples containing IRD do not deviate from the \overline{SS} -SS% trend (Figure S2a).

Supplementary Figures

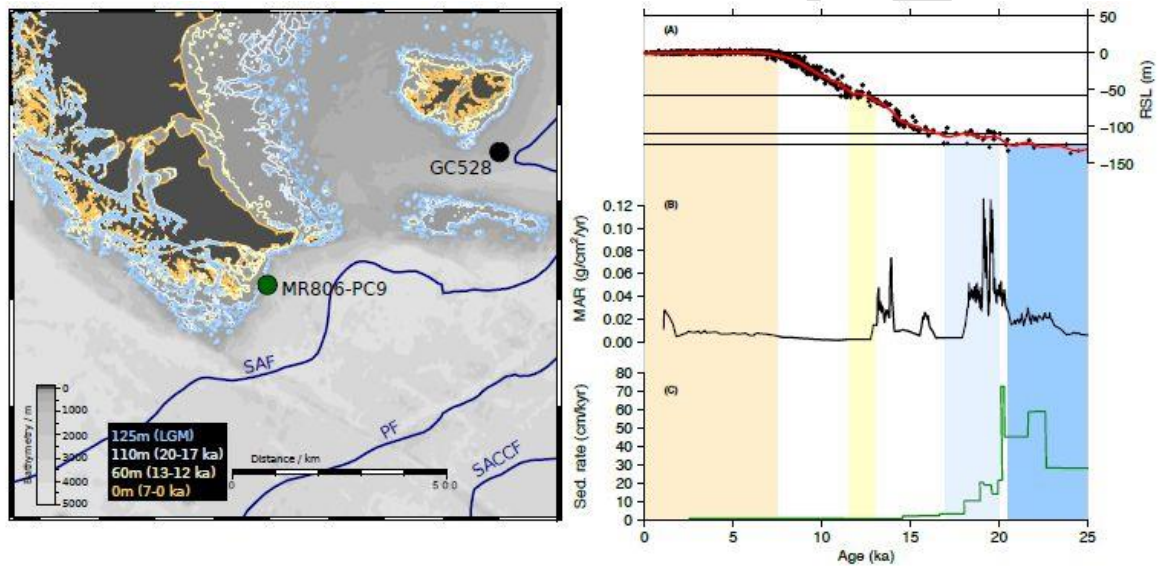
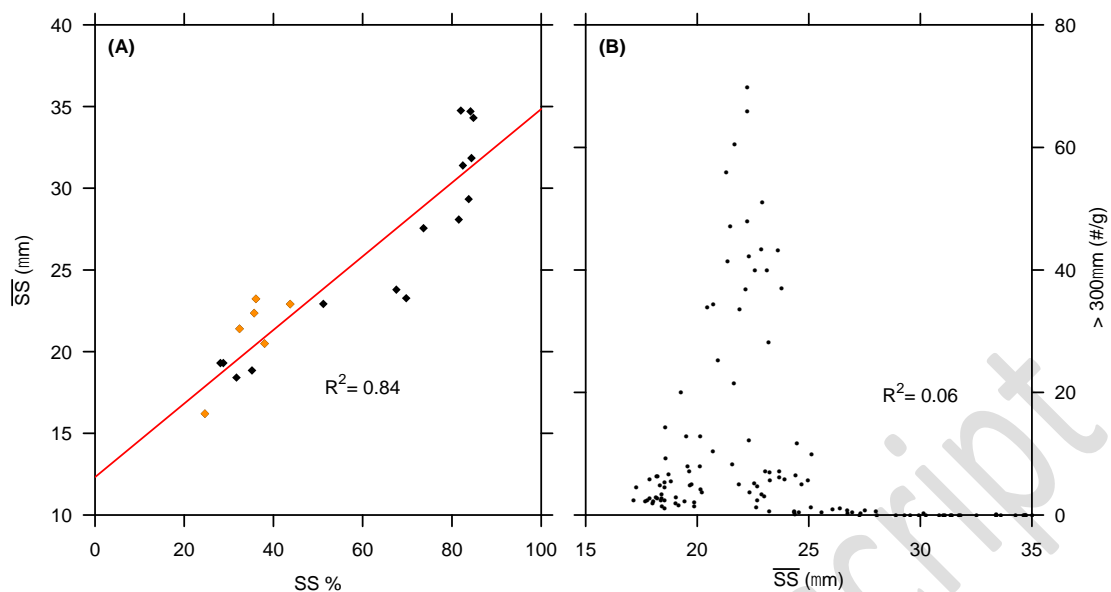


Figure S1: Assessing the impact of changes in sea level on the patterns of sedimentation. (Left) Map showing the position of the coastline at various intervals during the last deglaciation (see inset box) based on bathymetry. (Right) (A) Global relative sea level change over the last deglaciation (Lambeck et al., 2014); (B) Mass accumulation rate at site GC528; (C) Sedimentation rate at site MR806-PC9 (Lamy et al., 2015).



748

749 **Figure S2:** Assessing the current sorting in core GC528. (A) Cross-plot of weight percentage sortable
 750 silt fraction (10-63μm) versus the mean sortable silt grain size. Samples that contain significant
 751 quantities of IRD (grains > 300μm) are shown in orange. (B) Cross-plot of mean sortable silt grain size
 752 versus IRD (grains > 300μm) concentration.

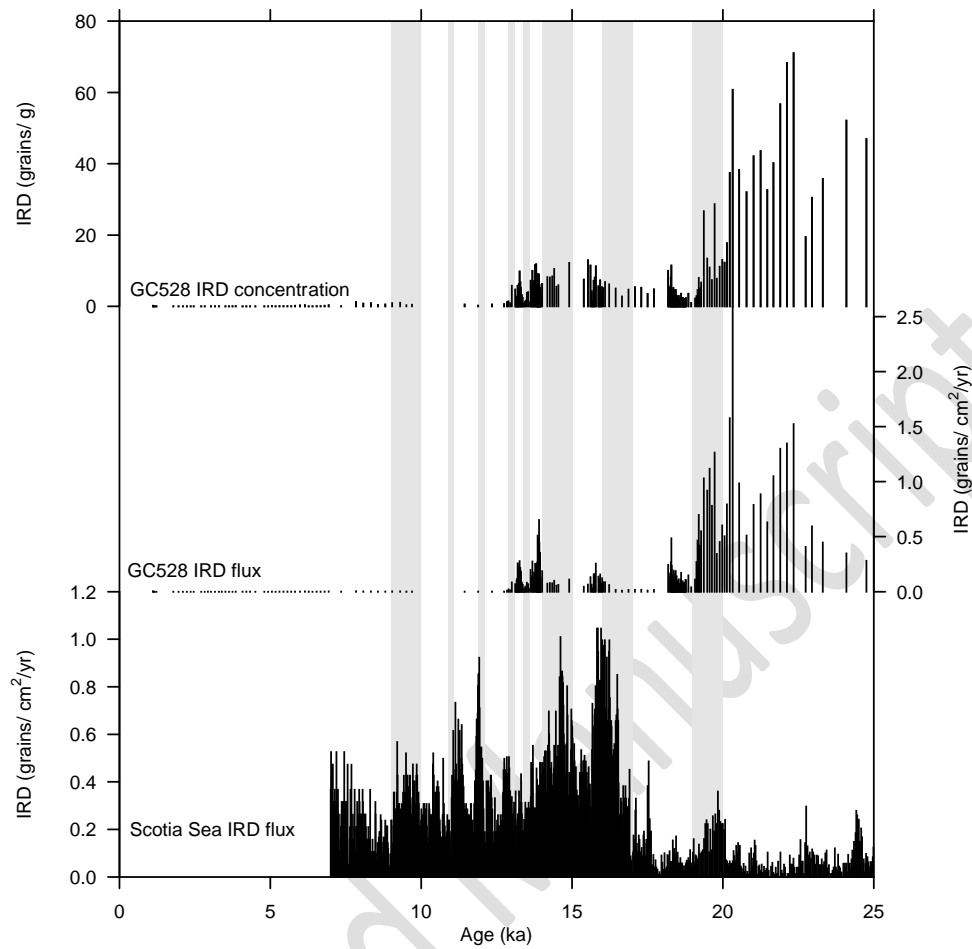


Figure S3: Comparison of the IRD records from the Southwest Atlantic (GC528) and the Scotia Sea (Weber et al., 2014). (A) GC528 IRD concentration; (B) GC528 IRD flux (based on mass accumulation rates); (C) Scotia Sea IRD flux. Grey bars show the Antarctic Icesheet Discharge events (AIDS; Weber et al., 2014)

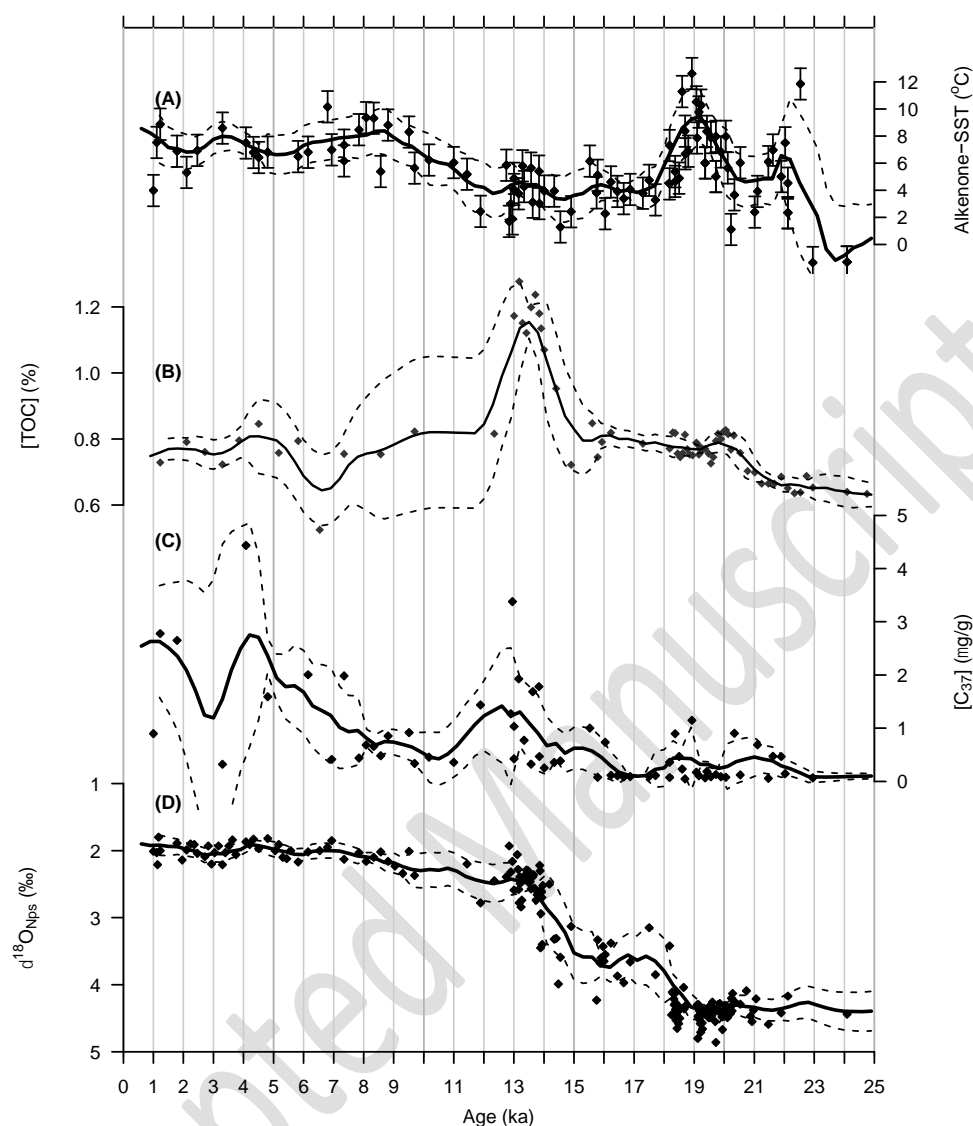


Figure S4: Assessing the potential for reworked alkenones having affected the LGM alkenone-SST record. (A) Alkenone-derived SST records from downstream (GC528 - black) of the Drake Passage; (B) Total organic carbon concentration in GC528; (C) Total alkenone concentration in GC528; (D) Planktonic foraminifera *Neoglobobadrina pacherma* (*sinistral*) $\delta^{18}\text{O}$ from GC528.

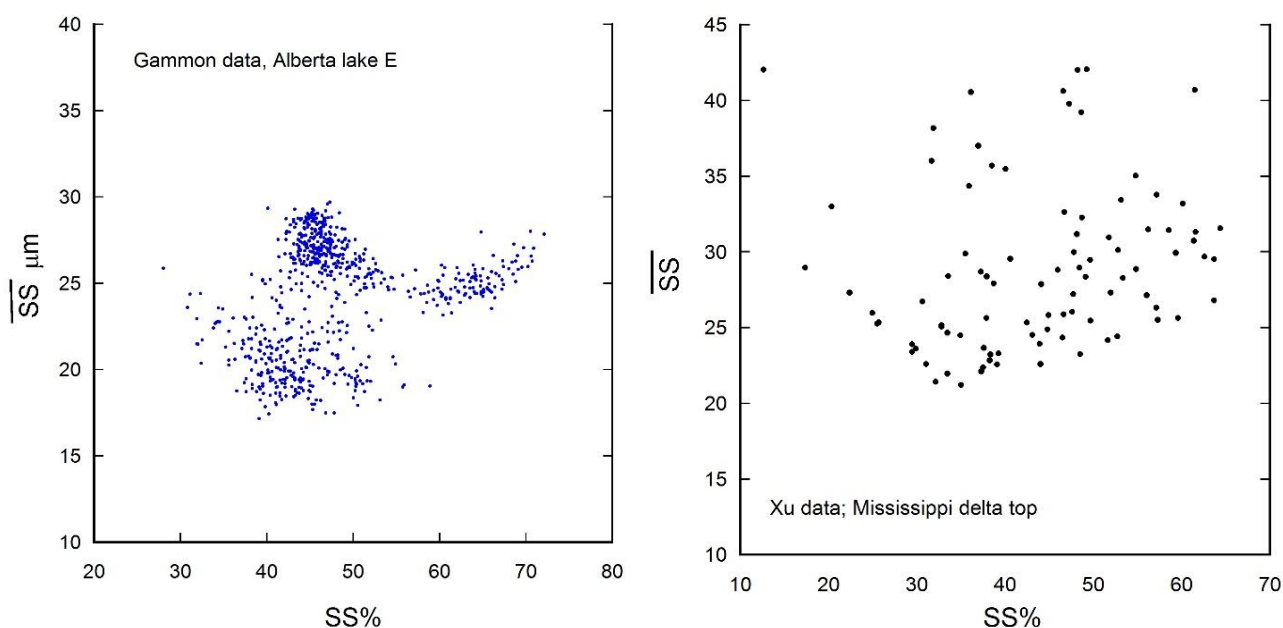


Figure S5: Unsorted sediment cross-plots from the fluvially dominated Alberta Lake (left; Gammon et al., 2017) and the Mississippi delta top (right; Xu et al., 2016)

References

- Einstein, H.A., Krone, R.B., 1962. Experiments to determine modes of cohesive sediment transport in salt water. *J. Geophys. Res.* 67, 1451–1461.
- Gammon, P.R., Neville, L.A., Patterson, R.T., Savard, M.M., Swindles, G.T., 2017. A log-normal spectral analysis of inorganic grain-size distributions from a Canadian boreal lake core: Towards refining depositional process proxy data from high latitude lakes. *Sedimentology* 64, 609–630. doi:10.1111/sed.12281
- Krone, R.B., 1962. Flume studies of the transport of sediment in estuarial shoaling processes, Final Report, Hydraulic Engineering Laboratory and Sanitary Engineering Research Laboratory, University of California.
- Lambeck, K., Rouby, H., Purcell, A., Sun, Y., Sambridge, M., 2014. Sea level and global ice volumes from the Last Glacial Maximum to the Holocene. *Proc. Natl. Acad. Sci. U. S. A.* 111, 15296–15303. doi:10.1073/pnas.1411762111
- Lamy, F., Arz, H.W., Kilian, R., Lange, C.B., Lembke-Jene, L., Wengler, M., Kaiser, J., Baeza-Urrea, O., Hall, I.R., Harada, N., Tiedemann, R., 2015. Glacial reduction and millennial-scale variations in Drake Passage throughflow. *Proc. Natl. Acad. Sci. U. S. A.* 112, 13496–501. doi:10.1073/pnas.1509203112
- McCave, I.N., 2008. Size Sorting during transport and deposition of fine sediments. Sortable silt and flow speed, in: Rebesco, M., Camerlenghi, A. (Eds.), *Developments in Sedimentology*. Elsevier,

789 Amsterdam, pp. 121–142. doi:10.1016/S0070-4571(08)10008-5

790 McCave, I.N., 2007. Deep-sea sediment deposits and properties controlled by currents, in: Hillaire-
 791 Marcel, C., de Vernal, A. (Eds.), *Proxies in Late Cenozoic Paleoceanography*. Elsevier,
 792 Amsterdam, pp. 19–62. doi:10.1016/S1572-5480(07)01006-8

793 McCave, I.N., 2002. Sedimentary settings on continental margins - an overview, in: Wefer, G., Billet,
 794 D., Hebbeln, D., Jorgensen, B.B., Schlüter, M., van Weering, T.C.E. (Eds.), *Ocean Margin
 795 Systems*. Springer Berlin Heidelberg, Berlin, Heidelberg, pp. 1–14. doi:10.1007/978-3-662-
 796 05127-6_1

797 McCave, I.N., Hall, I.R., 2006. Size sorting in marine muds: Processes, pitfalls, and prospects for
 798 paleoflow-speed proxies. *Geochem., Geophys. Geosyst.* 7, 37pp. doi:10.1029/2006GC001284

799 McCave, I.N., Manighetti, B., Robinson, S.G., 1995. Sortable silt and fine sediment size/composition
 800 slicing: Parameters for palaeocurrent speed and palaeoceanography. *Paleoceanography* 10,
 801 593–610. doi:10.1029/94PA03039

802 Thomsen, L., Weering, T. van, Blondel, P., Lampitt, R., Lamy, F., McCave, N., McPhail, S., Mienert, J.,
 803 Neves, R., D'Ozouville, L., Ristow, D., Waldmann, C., Wollast, R., 2002. Margin building -
 804 regulating processes, in: Wefer, G., Billet, D., Hebbeln, D., Jorgensen, B.B., Schlüter, M., van
 805 Weering, T.C.E. (Eds.), *Ocean Margin Systems*. Springer, Berlin, Heidelberg, pp. 195–203.
 806 doi:10.1007/978-3-662-05127-6_12

807 Weber, M.E., Clark, P.U., Kuhn, G., Timmermann, A., Spreng, D., Gladstone, R., Zhang, X., Lohmann,
 808 G., Menviel, L., Chikamoto, M.O., Friedrich, T., Ohlwein, C., 2014. Millennial-scale variability in
 809 Antarctic ice-sheet discharge during the last deglaciation. *Nature* 510, 134–8.
 810 doi:10.1038/nature13397

811 Xu, K., Bentley, S., Robichaux, P., Sha, X., Yang, H., 2016. Implications of Texture and Erodibility for
 812 Sediment Retention in Receiving Basins of Coastal Louisiana Diversions. *Water* 8, 26.
 813 doi:10.3390/w8010026

814